Constraints on the presence of post-perovskite in Earth's lowermost mantle from tomographic-geodynamic model comparisons

P. Koelemeijer [a,b,*], B.S.A. Schuberth [c], D.R. Davies [d], A. Deuss [e], J. Ritsema [f]

[a] *University College Oxford, Department of Earth Sciences, University of Oxford, Oxford, United Kingdom*
[b] *Institute of Geophysics, Department of Earth Sciences, ETH Zürich, Zurich, Switzerland*
[c] *Geophysics Section, Department of Earth and Environmental Sciences, Ludwig-Maximilians-Universität München, Munich, Germany*
[d] *The Research School of Earth Sciences, Australian National University, Canberra, Australia*
[e] *Department of Earth Sciences, Utrecht University, Utrecht, The Netherlands*
[f] *Department of Earth and Environmental Sciences, University of Michigan, Ann Arbor, USA*

ARTICLE INFO

ABSTRACT

Lower mantle tomography models consistently feature an increase in the ratio of shear-wave velocity (V_S) to compressional-wave velocity (V_P) variations and a negative correlation between shear-wave and bulk-sound velocity (V_C) variations. These seismic characteristics, also observed in the recent SP12RTS model, have been interpreted to be indicative of large-scale chemical variations. Other explanations, such as the lower mantle post-perovskite (pPv) phase, which would not require chemical heterogeneity, have been explored less. Constraining the origin of these seismic features is important, as geodynamic simulations predict a fundamentally different style of mantle convection under both scenarios. Here, we investigate to what extent the presence of pPv explains the observed high V_S/V_P ratios and negative V_S–V_C correlation globally. We compare the statistical properties of SP12RTS with the statistics of synthetic tomography models, derived from both thermal and thermochemical models of 3-D global mantle convection. We convert the temperature fields of these models into seismic velocity structures using mineral physics lookup tables with and without pPv. We account for the limited tomographic resolution of SP12RTS using its resolution operator for both V_S and V_P structures. This allows for direct comparisons of the resulting velocity ratios and correlations. Although the tomographic filtering significantly affects the synthetic tomography images, we demonstrate that the effect of pPv remains evident in the ratios and correlations of seismic velocities. We find that lateral variations in the presence of pPv have a dominant influence on the V_S/V_P ratio and V_S–V_C correlation, which are thus unsuitable measures to constrain the presence of large-scale chemical variations in the lowermost mantle. To explain the decrease in the V_S/V_P ratio of SP12RTS close to the CMB, our results favour a pPv-bearing CMB region, which has implications for the stability field of pPv in the Earth's mantle.

© 2018 Elsevier B.V. All rights reserved.

1. Introduction

Tomographic models typically display an increase in the ratio of shear-wave velocity variations ($\mathrm{dln}V_S = \delta V_S/V_S$) to compressional-wave velocity variations ($\mathrm{dln}V_P$) up to values of 2.5–3.5 in the lowermost mantle, accompanied by a strong negative correlation between shear-wave and bulk-sound velocity variations ($\mathrm{dln}V_C$) (e.g. Su and Dziewonski, 1997; Ishii and Tromp, 1999; Masters et al., 2000; Della Mora et al., 2011; Koelemeijer et al., 2016). The depth extent of these seismic features varies (Fig. 1). Models based on body-wave data typically show high ratios throughout the lower mantle, whereas models based on longer period data feature lower ratios. Model SP12RTS contains a marked decrease in the ratio near the core–mantle boundary (CMB), a robust feature due to the incorporation of CMB Stoneley mode data (Koelemeijer et al., 2016).

Traditionally, observations of a high ratio of $\mathrm{dln}V_S$ over $\mathrm{dln}V_P$ (from hereon termed *S/P ratio*) and a negative correlation between $\mathrm{dln}V_S$ and $\mathrm{dln}V_C$ (from hereon termed *S–C correlation*) have been interpreted as evidence for compositional heterogeneity (e.g. Su and Dziewonski, 1997; Masters et al., 2000; Moulik and Ekström, 2016), as purely thermal effects (in the absence of temperature-dependent phase changes) only produce a S/P ratio of up to ~2.5 (Karato and Karki, 2001). Specifically, two large-low-velocity provinces (LLVPs) underneath the Pacific and Africa, which cover ~25 percent of the core surface, are thought to be chemically distinct, as these feature the largest increase in the S/Pratio,
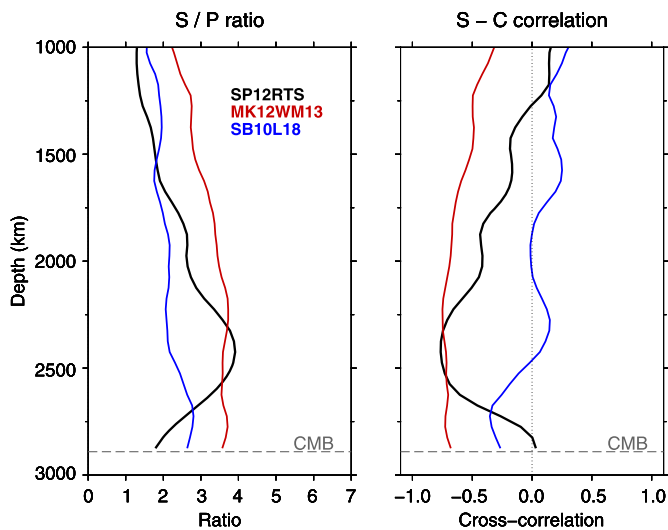
Fig. 1. Characteristics of global tomography showing the S/P ratio (left) and S–C correlation (right) for some extreme cases: body-wave model MK12WM13 of Su and Dziewonski (1997) (red), long-period model SB10L18 of Masters et al. (2000) (blue) and mixed-data model SP12RTS of Koelemeijer et al. (2016) (black). (For interpretation of the colours in the figure(s), the reader is referred to the web version of this article.)

have a pronounced negative S–C correlation (Masters et al., 2000; Koelemeijer et al., 2016) and show a large deviation from purely thermal velocity variations (Simmons et al., 2010; Tesoniero et al., 2016). In the past, this interpretation has been corroborated by normal-mode density models that indicated that the LLVPs have a higher-than-average density (Ishii and Tromp, 1999; Trampert et al., 2004). However, recent studies have found both dense (Moulik and Ekström, 2016; Lau et al., 2017) and light LLVPs (Koelemeijer et al., 2017). Determining the origin of the large-scale LLVPs is important, as isochemical and thermochemical convection models predict distinct thermochemical evolutionary pathways, different geochemical residence times, a contrasting distribution and magnitude of CMB heat flow, and, hence, models of outer core convection.

Before observations of a high S/P ratio and negative S–C correlation can be interpreted as solely due to chemical heterogeneity, other mechanisms need to be considered. As suggested in the past (Tsuchiya et al., 2004; Wookey et al., 2005), the lower mantle post-perovskite phase (pPv) also provides an possible explanation for these seismic features without the need for large-scale chemical variations. An increase in V_S and a decrease in V_P accompanies the phase transition from bridgmanite (brg) to pPv (e.g. Murakami et al., 2004; Oganov and Ono, 2004; Tsuchiya et al., 2004), resulting in an increased S/P ratio and a negative S–C correlation. In addition, the presence of a phase transition introduces artefacts in radially-averaged depth profiles of seismic velocities and their ratios (Styles et al., 2011). Although, in principle, the properties of pPv thus explain seismic characteristics of global tomography models (Davies et al., 2012, 2015), its stability field is composition-dependent and remains poorly constrained by mineral physics (Cobden et al., 2014). In addition, it has not been investigated yet whether: (i) the occurrence of pPv is expected to be widespread enough to influence radially-averaged seismic properties; (ii) the effect of pPv is observable in large-scale global tomography models; and thus whether (iii) global tomography can be used to constrain its stability field.

Here, we aim to establish whether the presence of pPv or chemical heterogeneity is the dominant factor in explaining the globally observed high S/P ratio and negative S–C correlation in the lowermost mantle. In addition, we investigate whether global tomography can provide insights into the stability field of post-

perovskite. To this end, we study the seismic properties of geodynamic models with and without pPv, and compare these to seismic tomography models. As in previous studies (Schuberth et al., 2009a; Davies et al., 2012), we ensure that our comparisons are meaningful, especially in terms of the amplitudes, by utilising a tomographic resolution operator (Ritsema et al., 2007). Although studies have filtered V_S structures in the past, using for example the resolution operator of S40RTS (Ritsema et al., 2011), joint filters for V_S and V_P structures are not readily available. Here, we use the resolution operator of SP12RTS (Koelemeijer et al., 2016), which filters both $dlnV_S$ and $dlnV_P$ structures simultaneously and has an improved resolution close to the CMB due to the inclusion of Stoneley mode data. Therefore, comparisons of SP12RTS with filtered geodynamic models enable us to investigate the origin of the high S/P ratio near 2500 km depth, its decrease towards the CMB and the negative S–C correlation in the lowermost mantle.

This paper is organised as follows: In Section 2, we provide a brief description of model SP12RTS and the geodynamic models used in this study, before introducing the SP12RTS tomographic resolution operator (Section 2.3). Subsequently, we discuss the effects of reparameterisation and tomographic filtering on synthetic tomography models in Section 3, demonstrating that the effect of pPv remains evident throughout these processing steps. In Section 4 we compare SP12RTS with the geodynamic models, discuss their properties as well as the important effects of data weighting and the Clapeyron slope in the tomographic inversions. These comparisons indicate that pPv plays a dominant role in explaining lowermost mantle characteristics of global seismic tomography models, even within the LLVPs. Finally, in Section 5 we discuss the implications of our results in light of the current state of knowledge in mineral physics, showing that tomographic-geodynamic comparisons can potentially be used to constrain the stability field of pPv.

2. Model specifications and resolution operator

We briefly review model SP12RTS and the geodynamic models explored in this study. We refer the reader to Koelemeijer et al. (2016) for further details on model SP12RTS and to Schuberth et al. (2009b) and Davies et al. (2012) for a more extensive discussion of the geodynamic modelling and mineral physics conversions.

2.1. Seismic model SP12RTS

SP12RTS is a whole-mantle, long-wavelength model of shear-wave and compressional-wave velocity variations, obtained using the same inversion procedure as S-wave velocity model S40RTS (Ritsema et al., 2011). To optimise data coverage, normal-mode splitting function measurements, Rayleigh wave phase-velocity measurements and teleseismic body-wave traveltimes were combined, with varying weighting factors between the three data sets. Compared to S40RTS, P-wave traveltime data were added and the normal-mode splitting function data set was significantly increased (143 modes instead of 49). By including 33 new modes sensitive to V_P variations, as well as 9 CMB Stoneley modes with an unique sensitivity to the lowermost mantle (Koelemeijer et al., 2013), P-wave velocity variations were independently constrained in the inversion. The model was parameterised laterally in spherical harmonics up to angular order 12, limiting us to consider large-scale structure only.

Fig. 2 shows the velocity structure of SP12RTS in the lowermost mantle. The long-wavelength V_S structure is practically identical to that of S40RTS, and SP12RTS contains many features observed in other tomographic models. Large regions of low shear- and compressional-wave velocities (LLVPs) exist underneath the Pacific and Africa, increasing in strength towards the CMB. The LLVP under
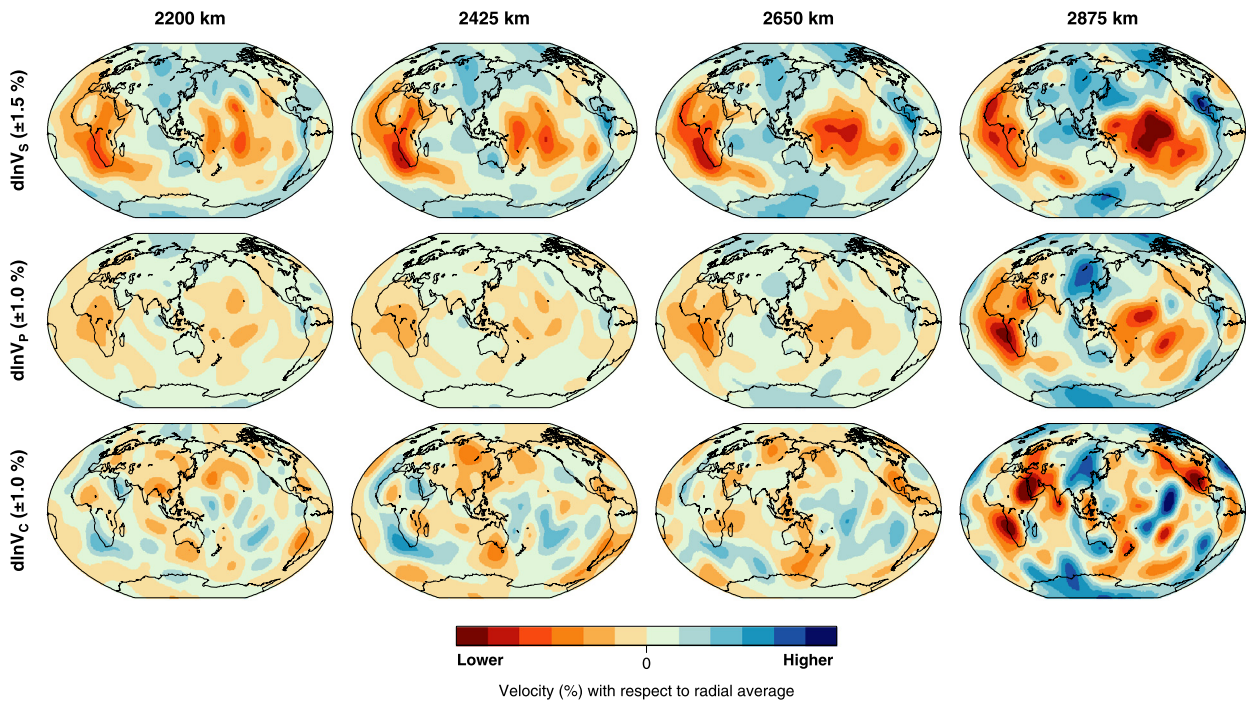
Fig. 2. Variations in shear-wave velocity $d\ln V_S$ (top), compressional-wave velocity $d\ln V_P$ (middle) and bulk-sound velocity $d\ln V_C$ (bottom) according to model SP12RTS at different depths in the mantle. Velocity is higher (lower) than the radial average at each depth in blue (red) regions and the colour intensity is proportional to the velocity amplitude up to a maximum of 1.5% for $d\ln V_S$ and 1.0% for $d\ln V_P$ and $d\ln V_C$, respectively. Note that $d\ln V_C$ are constructed using $d\ln V_S$ and $d\ln V_P$, thus giving rise to small-scale artefacts that should not be interpreted.

the Pacific is more circular, whereas the African LLVP is elongated in the North-South direction, and both are surrounded by a ring of higher velocities. V_S amplitudes increase continuously with depth, whereas V_P variations only increase from ∼2500 km depth. However, their geographic patterns are strongly correlated at all depths. The V_C variations, constructed using $d\ln V_S$ and $d\ln V_P$ following the method of Masters et al. (2000), are negatively correlated with V_S variations, both within and outside the LLVPs. The negative S–C correlation and S/P ratio peak at a depth of 2500 km before decreasing towards the CMB (Fig. 1). Although such a decrease had been observed previously (Romanowicz, 2001; Della Mora et al., 2011), it was generally attributed to poor data coverage near the CMB. However, in case of SP12RTS, Koelemeijer et al. (2016) showed that this is a robust feature due to the incorporation of CMB Stoneley modes.

2.2. Geodynamic models

We use high-resolution global mantle circulation models similar to those presented in Schuberth et al. (2009b) and Davies et al. (2012). We generate temperature and compositional fields using a modified and benchmarked version of the spherical mantle convection code TERRA (Baumgardner, 1985; Davies et al., 2013), which solves for the conservation equations of mass, momentum and energy at infinite Prandtl number (i.e. no inertial forces). We prescribe isothermal conditions at the surface (300 K) and CMB (4000 K). We specify a free slip boundary condition at the CMB, while we prescribe surface velocities according to 200 Myr of plate motion history (Seton et al., 2012), at discrete 1 Myr intervals. A fine discretisation (∼25 km cells, resulting in about 80 million grid points) allows us to simulate mantle flow at Earth-like convective vigour, which is essential for generating synthetic structures that are comparable to seismic observations of Earth's present-day mantle. Our models include internal heating in the mantle, compressibility and a temperature-depth dependent viscosity. The Supplementary Material contains further details on these parameters

and the model initiation procedure, with key model parameters listed in Supplementary Table S1.

Similarly to Davies et al. (2012), we focus on two end-member scenarios for describing temperature variations within the mantle: (i) a purely thermal model with no chemical heterogeneity ('TH' models from hereon); and (ii) a thermochemical 'pile' model, where chemically distinct material focuses into large-scale structures in the lowermost mantle ('TC' models from hereon). We convert modelled temperature, pressure and compositional fields into elastic parameters using lookup tables generated with a thermodynamic mineralogical model for a simplified six-component system of mantle composition (Stixrude and Lithgow-Bertelloni, 2011). We opt to use such a self-consistent mineralogical model, where the thermodynamics of the system dictate the stability field of pPv and thus its Clapeyron slope, instead of assuming a constant Clapeyron slope (see Supplementary Fig. S1 and Supplementary Material). This way, we incorporate the non-linear pressure and temperature dependence of material properties and account for non-linear thermodynamic effects on phase transitions.

We perform the conversion using two versions of the lookup tables for each chemical composition, one including and the other excluding pPv from the database. Hence, we obtain four synthetic tomography models: models TH-pPv and TC-pPv where pPv is included, and models TH-nopPv and TC-nopPv where pPv is not present in the lowermost mantle. For TH-pPv models, we also test the influence of the assumed Clapeyron slope using extrapolated (i.e. not physically constrained) mineral physics tables, described in more detail in the Supplementary Material. In the conversion, we assume a pyrolitic mantle composition for the TH models, whereas TC models contain an additional basalt component, which comprises ∼3% of the mantle's volume (see Supplementary Table S2). We do not include the dynamic effects of the post-perovskite transition in the geodynamic simulations themselves, only at the conversion stage to seismic velocities. However, as we limit ourselves to the interpretation of large-scale statistical properties, we do not

expect our results to change significantly (see Supplementary Material).

Fig. 3 illustrates present-day snapshots of the temperature field, V_S structure and pPv occurrence in the geodynamic models in the lowermost mantle. Remnants of old slabs are visible above the CMB in all models. These downwellings modulate the location of hot material such that it becomes concentrated into large-scale structures beneath Africa and the Pacific. The Pacific anomaly is approximately circular, while the African anomaly is a NW–SE trending structure, extending southeastwards into the Indian Ocean. In TH models, these structures comprise clusters of plumes and interconnected hot (slow), linear ridges, whereas in TC models they represent discontinuous chemical 'piles'. These piles cover around 40% of the CMB, with the highest temperatures (lowest S-wave velocities) predicted at their edges. At ∼2480 km depth, pPv is present locally in high-velocity regions (pyrolite composition) in both TH and TC models, resulting in increased V_S amplitudes. With depth, its occurrence becomes more wide-spread and the mineral physics tables predict that pPv is present everywhere at ∼2750 km depth, even for basaltic material (see Supplementary Fig. S1). We observe the strongest velocity variations around 2575 km depth, where large regions of bridgmanite material transform to post-perovskite. These large velocity variations are due to the removal of the radial average at each depth and expected for a phase transition (Styles et al., 2011). The presence of pPv affects V_P variations in a similar way, except that it reduces their amplitudes rather than increasing them (Supplementary Fig. S2).

2.3. Seismic resolution operator

Following Ritsema et al. (2007), we define the resolution operator $\mathcal{R} = \mathbf{G}^{\dagger}\mathbf{G}$, where $\mathbf{G}$ is the operator of the seismic forward problem and $\mathbf{G}^{\dagger}$ is its generalised inverse. We modify the geodynamic prediction of seismic heterogeneity (the "true" input model $\mathbf{m^{IN}}$) by multiplying it with $\mathcal{R}$ to obtain a "filtered" output model $\mathbf{m^{OUT}}$ as if imaged by tomographic inversion:

$$\mathbf{m^{OUT}} = \mathcal{R}\mathbf{m^{IN}}. \tag{1}$$

$\mathcal{R}$ fully describes the spatially heterogeneous resolution of the tomographic model. We have to compute $\mathcal{R}$ on the basis of the same damping parameter ϵ as the tomographic model. In SP12RTS, ϵ was 0.005, corresponding to ∼1200 unknowns, which we therefore adopt here as well.

In contrast to S40RTS, SP12RTS is a tomographic model of both V_S and V_P variations, hence the model vector $\mathbf{m}$ consists of two parts:

$$\mathbf{m} = \begin{pmatrix} \mathbf{S} \\ \mathbf{P} \end{pmatrix}, \tag{2}$$

where $\mathbf{S}$ and $\mathbf{P}$ are model vectors describing $\mathrm{dln}V_S$ and $\mathrm{dln}V_P$, respectively. We rewrite Equation 1 as follows:

$$\begin{pmatrix} \mathbf{S^{OUT}} \\ \mathbf{P^{OUT}} \end{pmatrix} = \begin{pmatrix} \mathcal{R_{SS}} & \mathcal{R_{SP}} \\ \mathcal{R_{PS}} & \mathcal{R_{PP}} \end{pmatrix} \begin{pmatrix} \mathbf{S^{IN}} \\ \mathbf{P^{IN}} \end{pmatrix}, \tag{3}$$

where $\mathcal{R_{SS}}$ and $\mathcal{R_{PP}}$ are the diagonal blocks of $\mathcal{R}$ detailing how V_S structure maps into V_S structure (ditto for V_P). The off-diagonal blocks of $\mathcal{R}$, i.e. $\mathcal{R_{SP}}$ and $\mathcal{R_{PS}}$, contain information about how V_S and V_P structures map into each other (i.e. leakage of structure).

The resolution operator is dominantly diagonal (Koelemeijer et al., 2016), but $\mathcal{R_{SP}}$ and $\mathcal{R_{PS}}$ are not strictly zero. Therefore, some artefacts arise during tomographic filtering. Hence, it is crucial to use the full resolution operator incorporating the off-diagonal blocks when filtering geodynamic models. We note that the resolution of SP12RTS in the lower mantle is similar for $\mathrm{dln}V_S$ and $\mathrm{dln}V_P$, which is important when considering their ratio.

3. Effects of tomographic filtering on the S/P ratio and S–C correlation

To ensure meaningful comparisons – geodynamic models contain typically ∼80 million grid points, whereas SP12RTS was constructed with only ∼3500 parameters – we first have to reparameterise all original geodynamic models to the SP12RTS parameterisation (i.e. 21 splines with depth and spherical harmonics up to degree 12). Reparameterisation leads to a drastic reduction in the model dimensionality, broadening structures and reducing amplitudes of negative anomalies (low velocities) more (∼20–50% lower) than those of positive anomalies (∼0.5–15% lower) (Fig. 4a–b). Subsequently, we multiply the reparameterised models with $\mathcal{R}$, which effectively acts as a low-pass filter (Ritsema et al., 2007; Schuberth et al., 2009a), causing structures to broaden and weaken further (Fig. 4c). As the reparameterisation and filtering affect V_S and V_P structure differently in different locations, we explicitly consider here their effects on the S/P ratio and S–C correlation.

3.1. Global properties

In this paper, we always compute the velocity ratios and correlations with respect to each model's radial average. In addition, we consistently compute them using the spherical harmonic coefficients where possible, which allows us to consider different spherical harmonic degrees directly. For the high-resolution models, which are not parameterised in spherical harmonics, we use the RMS velocities, which results generally in the same curves (Koelemeijer et al., 2016). The resulting values are larger compared to using the median of the distribution (Koelemeijer et al., 2016). However, we prefer this approach as it means we do not divide by small values, which require special treatment (Tesoniero et al., 2016).

The presence of pPv is evident in the depth profiles of the original geodynamic models (Fig. 5a). At lowermost mantle depths where bridgmanite and pPv coexist (i.e. lateral variations in the presence of pPv occur), the S/P ratio increases and we observe a pronounced, negative S–C correlation. Both the S/P ratio and the S–C correlation curves peak around 2650 km depth, when most material has transformed to pPv. We only observe a single peak in the S/P ratio, rather than the typical peak-trough behaviour of a phase transition (Styles et al., 2011), as the RMS velocities are always positive.

Upon reparameterisation (Fig. 5b), minor artefacts are present in the model with pPv, because the smooth spline interpolation cannot capture the sharp depth changes in the ratio and correlation. We find stronger artefacts after tomographic filtering (Fig. 5c), primarily due to the non-zero off-diagonal terms of $\mathcal{R}$. This especially affects the S–C correlation as we construct $\mathrm{dln}V_C$ using $\mathrm{dln}V_S$ and $\mathrm{dln}V_P$, both with their own limited resolution. For model TH-pPv, the filtering results in a negative S–C correlation at depths as shallow as ∼1800 km. In addition, the thermal model without pPv (TH-nopPv), originally displaying a positive S–C correlation, now displays a small, negative S–C correlation that is entirely artificial. When we consider degree 2 structure only, artefacts are smaller and the S–C correlation of model TH-nopPv remains positive (Fig. 5c).

Despite the artefacts mentioned above, the effect of pPv remains evident throughout the processing steps, even when we account for the limited tomographic resolution. We consistently observe a high S/P ratio and negative S–C correlation due to pPv in the TH models, as also noted by Della Mora et al. (2011). The same trends are observed for TC models (Supplementary Fig. S3), although the presence of additional basalt material in the lowermost mantle complicates the patterns. On the contrary, the corre-
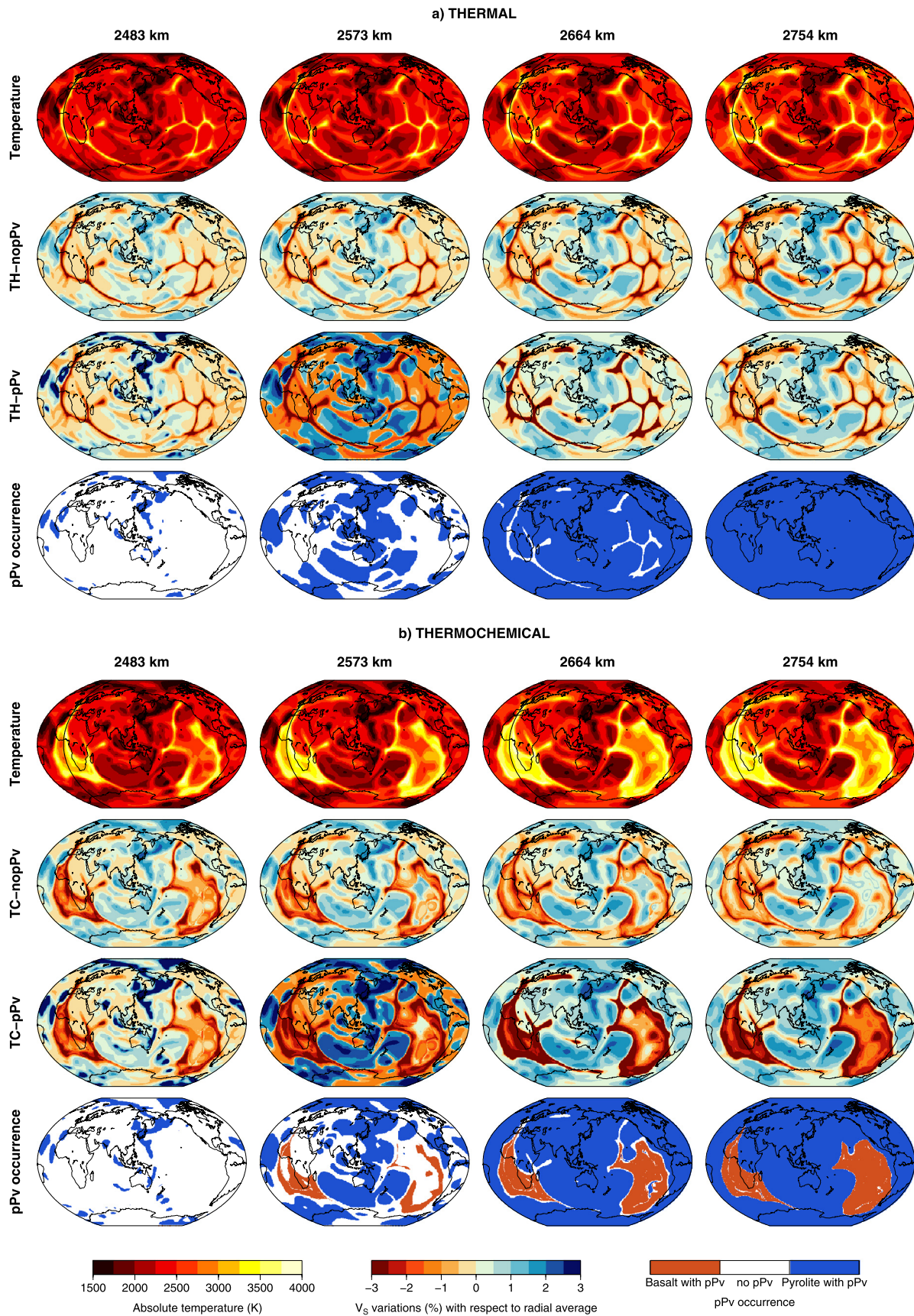
Fig. 3. Temperature, shear-wave velocity variations and pPv occurrence maps for (a) thermal (TH) models and (b) thermochemical (TC) models at different depths in the lowermost mantle. In each case, the top row shows the absolute temperature field (generated by the geodynamic modelling), the middle rows show the V_S structure (based on the mineral physics conversion) without and with pPv present, respectively, and the bottom row shows the lateral variations in pPv occurrence. For the shear-wave velocity variations, we remove the radial average at each depth.
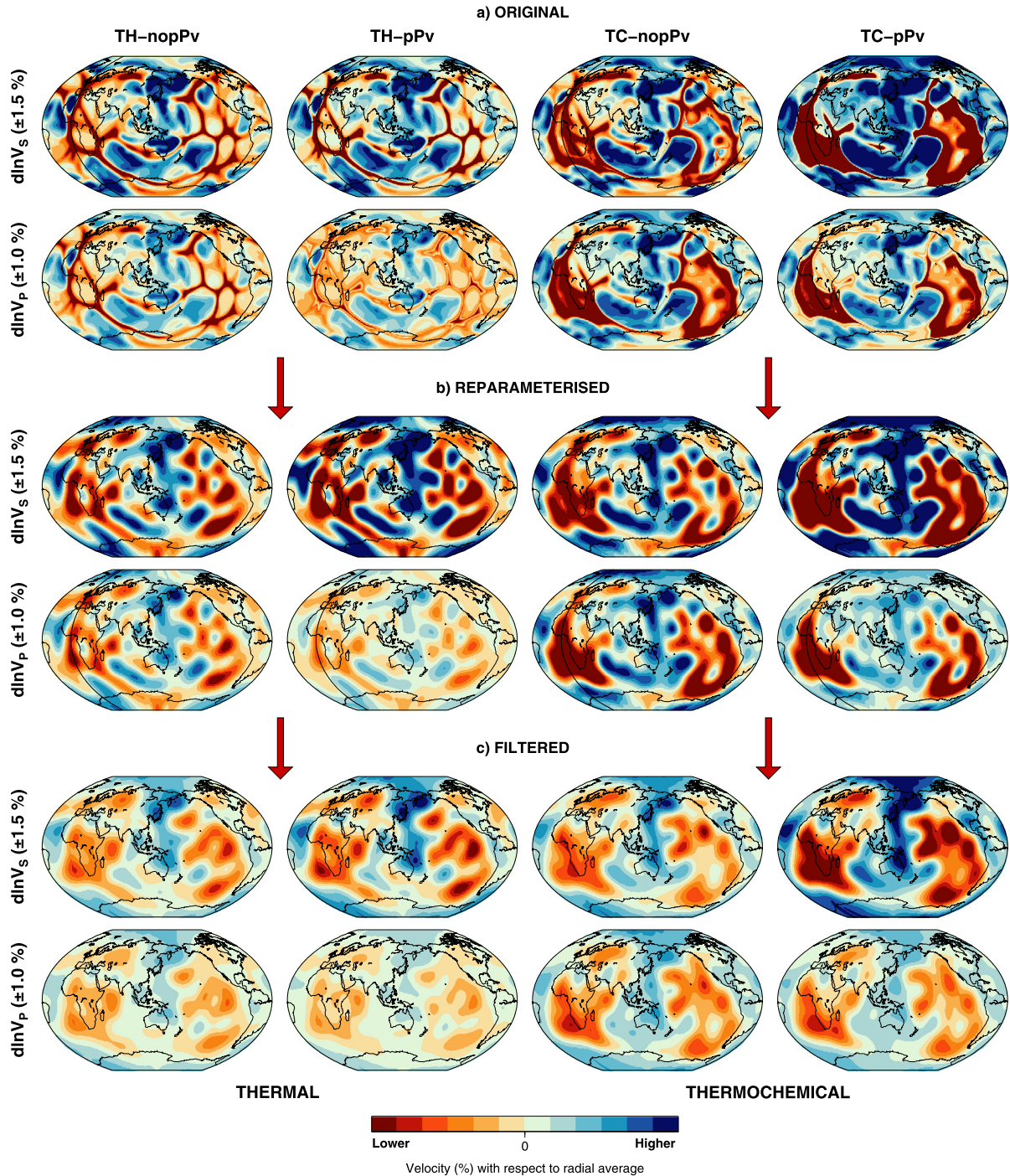
Fig. 4. dlnV_S (top) and dlnV_P (bottom) at 2650 km depth for (a) the original high-resolution geodynamic models, (b) the reparameterised geodynamic models and (c) the tomographically filtered geodynamic models. The colour scale is the same as in Fig. 2 with a maximum amplitude of 1.5% for dlnV_S and 1.0% for dlnV_P. The reparameterisation affects dlnV_S and dlnV_P structures in a similar way. Subsequently, the multiplication with $\mathcal{R}$ decreases both fast and slow anomalies by ∼35–50%, consistent with findings by (Zaroli et al., 2017). The effect of pPv remains evident after filtering, with models including pPv showing larger amplitudes for dlnV_S and lower amplitudes for dlnV_P.

lation between dlnV_S and dlnV_P (S–P correlation) is high in all geodynamic models, even after filtering (Supplementary Fig. S4). Therefore, we cannot use this property to probe for the presence of pPv and/or chemical heterogeneity.

3.2. Fast and slow clusters

For lowermost mantle structure, clusters of fast and slow velocities capture the differences between the LLVPs and the ambient mantle and thus provide more insights into the nature of seis-

mic anomalies (Lekić et al., 2012). As the Clapeyron slope of the brg-pPv phase transition is positive (Cobden et al., 2014), we expect the transition to occur at shallower depth in cold regions (fast velocities in TH models) than in hot regions (slow velocities). Consequently, the S/P ratio and S–C correlation peak at different depths in regions of fast and slow velocities, giving rise to a depth offset between the two. Here, we consider whether such a depth offset remains distinct after reparameterisation and filtering.
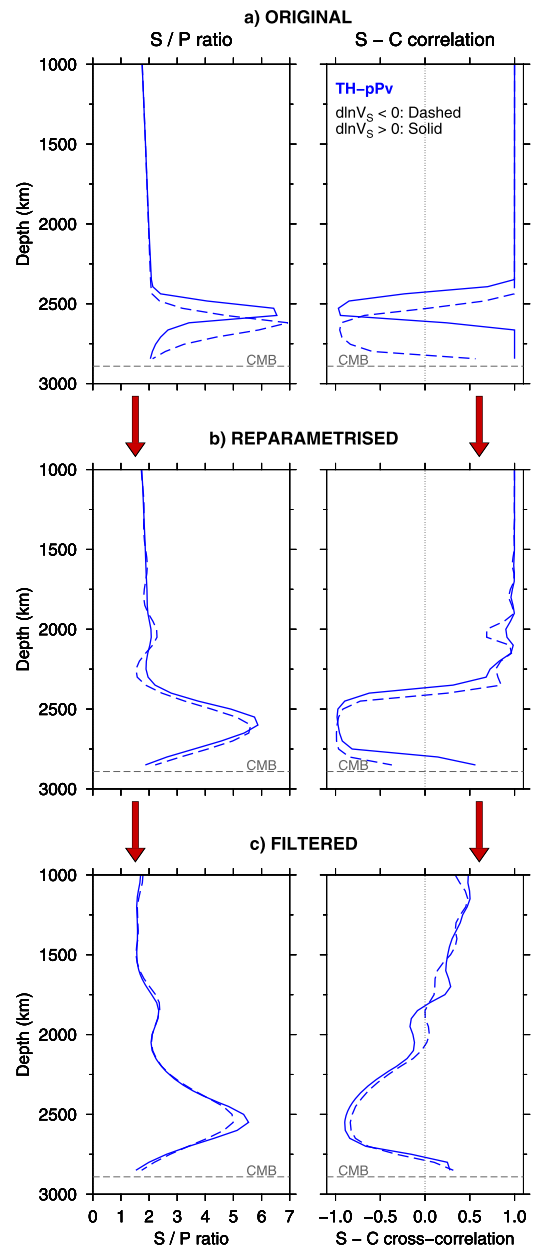
We split every geodynamic model into two clusters using the fast (dln$V_S > 0$) and slow (dln$V_S < 0$) anomalies of the models
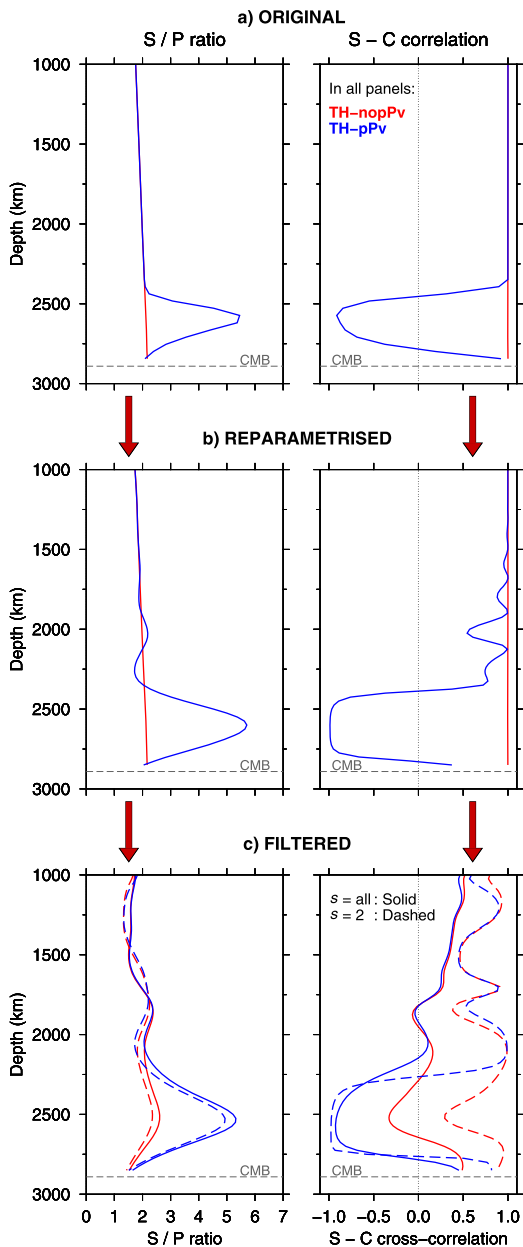
Fig. 5. Effects of reparameterisation and tomographic filtering on the S/P ratio (left) and S–C correlation (right) for thermal (TH) models. (a) Original high-resolution geodynamic models, (b) reparameterised geodynamic models and (c) tomographically filtered geodynamic models. Red and blue lines show thermal models without pPv (TH-nopPv) and with pPv (TH-pPv), respectively, with dashed lines in (c) indicating the degree 2 component only.
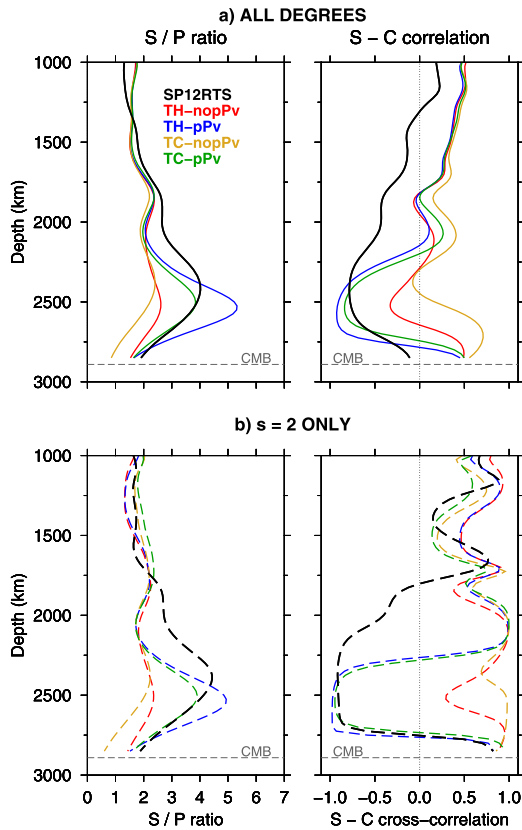
Fig. 6. The S/P ratio (left) and S–C correlation (right) in thermal model TH-pPv with post-perovskite present, separated into regions of fast (solid) and slow (dashed) shear-wave velocity variations. (a) Original high-resolution, (b) reparameterised, and (c) tomographically filtered geodynamic models.

themselves. We compute the geographic locations of both clusters at a reference depth of 2850 km and subsequently use this for all depths in the mantle, similar to Lekić et al. (2012). We exclude all points for which $dlnV_S$ or $dlnV_P$ are smaller than 0.01%. This approach is different from Koelemeijer et al. (2016) who split SP12RTS into fast and slow clusters using the vote map of Lekić et al. (2012). However, the vote map is based on the geographic distribution of seismic anomalies. Using the same approach for geodynamic models would not be meaningful, as the distribution of seismic structure depends on plate reconstructions and unknown initial conditions.

Using the cluster definition described above, original geodynamic models indeed feature a depth offset of ∼100 km between the fast and slow cluster, especially in the S–C correlation (Fig. 6).

After reparameterisation (Fig. 6b), the offset decreases (≤50 km) due to the broad spline spacing of SP12RTS in the lowermost mantle. Tomographic filtering removes this remaining depth offset, and we observe almost no difference in the filtered clusters (Fig. 6c). This implies that even if there is a depth offset between fast and slow velocity regions, it is not resolved by SP12RTS. It is thus not surprising that no depth offset was observed in SP12RTS itself (Koelemeijer et al., 2016). By incorporating a finer depth parameterisation, future studies may be able to improve on this.

4. Results

### 4.1. Tomographic-geodynamic model comparisons

The amplitudes of SP12RTS at 2650 km depth (Fig. 2, third column) are most compatible with those observed in filtered TH

Fig. 7. Comparison of the S/P ratio (left) and S–C correlation (right) between the geodynamic models and SP12RTS for (a) all spherical harmonic degrees up to $s = 12$ and (b) degree $s = 2$ only (dashed lines). Black lines show the characteristics of SP12RTS, whereas different colours represent the geodynamic models, as indicated in the figure.

Fig. 8. Comparison of the S/P ratio (left) and S–C correlation (right) calculated for (a) the fast cluster and (b) the slow cluster for all geodynamic models and SP12RTS. Colours are the same as in Fig. 7.

models (Fig. 4c), whereas the amplitudes in filtered TC models are too large (Davies et al., 2012), particularly for dlnV_P. Nevertheless, all geodynamic models reproduce the large-scale patterns of SP12RTS at this depth, with low velocity anomalies at the locations of the LLVPs, surrounded by higher-than-average velocities. We focus from hereon only on the S/P ratio and S–C correlation within a given model (computed directly from the spherical harmonic coefficients), removing the dependence on the plate reconstructions employed in the geodynamic simulations. We do not calculate tomographic-geodynamic model correlations, as these quantities would primarily inform us about the uncertainties in the plate reconstructions, rather than help us to constrain the origin of seismic anomalies.

Models with pPv match SP12RTS well below depths of ∼2300 km (Fig. 7) as they display an increased S/P ratio and a more negative S–C correlation in the lower mantle. However, the S/P ratio peaks ∼100 km deeper than in SP12RTS. Although models without pPv also feature a (small) negative S–C correlation (an artefact of the tomographic filtering as shown in the previous section), they fail to produce a high S/P ratio. The difference between models with and without pPv is particularly strong for degree-2 structure (Fig. 7b), where models with pPv are in close agreement with SP12RTS in the lowermost mantle (below ∼2300 km depth). Between 1700 km and 2300 km, all geodynamic models fail to reproduce the negative S–C correlation observed in SP12RTS. The addition of a chemically distinct phase (model TC-pPv) changes the amplitude of the S/P ratio, but it does not significantly improve the overall match with SP12RTS. Therefore, we conclude that both TH and TC models reproduce the main statistical properties of SP12RTS equally well, if pPv is present.
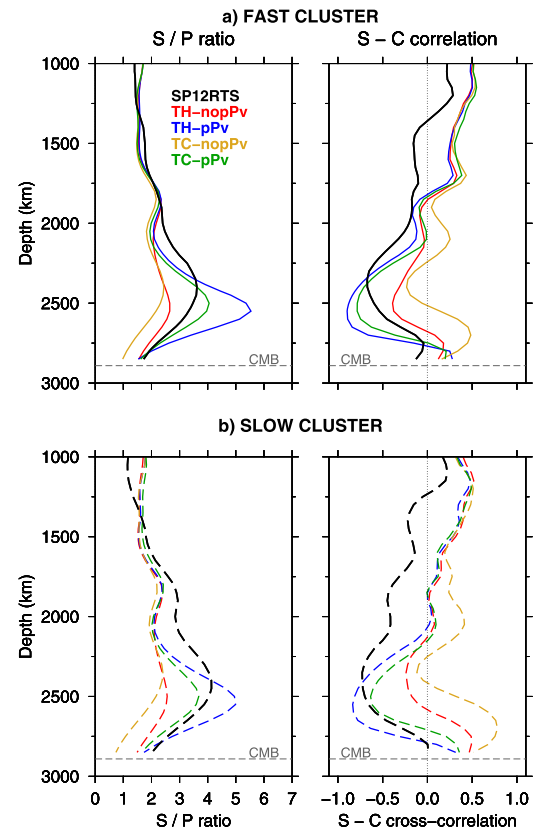
Although there is no difference between fast and slow clusters after tomographic filtering (Fig. 6), TH-pPv and TC-pPv (i.e. geodynamic models with pPv) reproduce the high S/P ratio and negative S–C correlation in both clusters and thus match the large-scale characteristics of SP12RTS (Fig. 8). Hence, pPv could also be used as an explanation for observations of a high S/P ratio and negative S–C correlation inside LLVPs, even though we expect these to be hotter than the surrounding mantle. However, one should keep in mind that the seismically slow regions (i.e. LLVPs) in filtered models also incorporate cold regions (i.e. with pPv) in the high-resolution models. Note also that pPv is not necessarily present at the same depths in both clusters (this depth sensitivity is lost during tomographic filtering). In addition, we have not imposed its presence in the LLVPs – this is a consequence of physically constrained dynamic models combined with mineral physics predictions for a reasonable mantle composition. Thus, our results merely imply that it is plausible for post-perovskite to be present within the seismically-imaged LLVPs and that its presence there explains tomographic features.

4.2. Effects of inversion data weighting

SP12RTS contains data from body waves, surface waves and normal modes, with weighting factors imposed between the different data sets. For the default SP12RTS model, the data weights were chosen to balance the sensitivities of body-wave and normal-mode data (Koelemeijer et al., 2016). To investigate the robustness of our results, we repeat our tomographic-geodynamic model comparison for inversions dominated either by normal-mode splitting functions or body-wave traveltimes. This means that we multiply our reparameterised models by $\mathcal{R}_s$ (normal-modes dominated) and
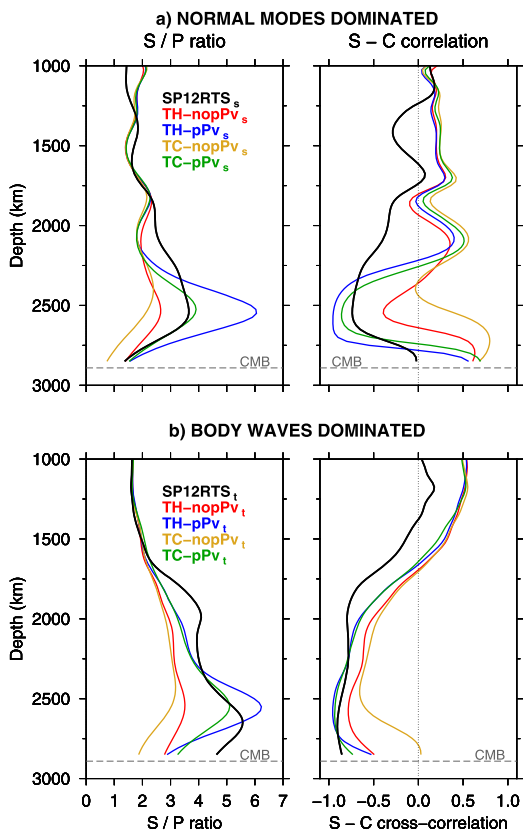
Fig. 9. Comparison of the S/P ratio (left) and S–C correlation (right) between geodynamic models and tomographic models obtained with different data weighting (i.e. SP12RTS$_s$ and SP12RTS$_t$ for inversions dominated by normal-mode and body-wave data, respectively), calculated for all spherical harmonic degrees. (a) Normal-mode data dominated inversion. (b) Body-wave data dominated inversion. The same colours as in Fig. 7 represent the geodynamic models, but we now filter them using either (a) $\mathcal{R}_s$ or (b) $\mathcal{R}_t$.

$\mathcal{R}_t$ (body-waves dominated) and compare these with the corresponding versions of SP12RTS (i.e. SP12RTS$_s$ and SP12RTS$_t$, respectively).

Models filtered using $\mathcal{R}_s$ (normal-modes dominated) show a clear difference due to the presence of pPv (Fig. 9a), with the best match again when pPv is present. For models filtered with $\mathcal{R}_t$ (body-waves dominated), we observe that the high S/P ratio and negative S–C correlation are artificially smeared upwards to depths of ∼2000 km for all models (Fig. 9b). A likely reason for this is that our filtering does not capture the uncertainties in the underlying theory of the tomographic inversion, in this case ray theory. Neglecting finite-frequency effects in combination with vertical ray paths thus leads to artificial high S/P ratios and a negative S–C correlation in the body-wave dominated inversions (Malcolm and Trampert, 2011). Thus, we argue that studies of the S/P ratio based on body-wave ray theory (e.g. Su and Dziewonski, 1997; Della Mora et al., 2011) cannot be used to distinguish between thermal and chemical variations, consistent with recent work by Tesoniero et al. (2016).

A spectral decomposition of model TH-pPv filtered using $\mathcal{R}_s$, $\mathcal{R}$ and $\mathcal{R}_t$ further illustrates the importance of the data weighting on the robust retrieval of the S/P ratio and S–C correlation (Supplementary Fig. S5). We recover the features of the reparameterised model (a high S/P ratio and negative S–C correlation at all spherical harmonic degrees) well using $\mathcal{R}_s$ (normal-mode dominated) for even spherical harmonic degrees. For SP12RTS (filtering using $\mathcal{R}$), we recover even degrees up to $l = 10$. However, the odd degrees display more artefacts, as the self-coupled splitting func-

tion data only constrain even-degree structure. When using $\mathcal{R}_t$ (body-waves dominated), we observe an increase in the S/P ratio at lowermost mantle depths and an artificial upward smearing of the negative S–C correlation to depths of 1800 km for all spherical harmonic degrees. This demonstrates that the depth extent of the negative S–C correlation depends on the weighting of the data sets, with more severe smearing occurring when we give more weight to body-wave data (if treated with ray theory). This is a possible explanation for the differences between previous tomographic models: the body-wave model of Su and Dziewonski (1997) featured a negative S–C correlation throughout the mantle, whereas the long-period model of Masters et al. (2000) only contained a negative correlation in the lowermost mantle (Fig. 1). We speculate that these studies imaged the same structures, filtered and smeared differently due to the differences in theoretical approximations in their respective inversion schemes.

4.3. Influence of the Clapeyron slope

The mineral physics table for pyrolite used here predicts that pPv is present everywhere at the CMB due to the shallowing of the Clapeyron slope at high temperature (see Supplementary Fig. S1). To test the influence of the Clapeyron slope on the S/P ratio and S–C correlation, as well as their fit to SP12RTS, we use two additional mineral physics tables as described in the Supplementary Material and shown in Fig. 10a. In these tables, "TH-pPv-extra" and "TH-pPv-extra100", we assume a constant Clapeyron slope of ∼13 MPa/K (i.e. the one found at low temperatures) and linearly extrapolate (i.e. non-physical) the phase boundary down to the CMB. This way, we enforce a pPv-free CMB while at shallower depth either pPv is everywhere except in the lowest velocity regions (TH-pPv-extra) or pPv only occurs as lenses in the highest velocity regions (TH-pPv-extra100) (Fig. 10b).

For the TH-pPv-extra model, we observe increased S/P ratios down to the CMB (Fig. 10c), whereas the TH-pPv-extra100 model results in lower S/P ratios. For both these models, the peak in the S/P ratio also occurs at greater depth as the stability field is shifted downwards. The different mineral physics tables produce a larger variation in the S/P ratio and S–C correlation compared to Fig. 7b. As the mineral physics tables are characterised by a different areal extent of pPv (Fig. 10b), we suggest that this areal extent has a strong control on the S/P ratio and S–C correlation, an idea we explore further in Section 5.1. We also note that even the effect of small lenses of pPv (the TH-pPv-extra100 model) is observable in the synthetic tomography images.

The shape of the S–C correlation curve for degree 2 is reproduced best by the original TH-pPv model, as the S–C correlation remains negative for the extrapolated tables (Fig. 10d). This is confirmed by calculating the L2-norm between the S/P ratio and S–C correlation curves of SP12RTS and the geodynamic models (Fig. 10e–f). Lower misfits are generally found when pPv has a larger areal extent (higher "pPv coverage") as in the original TH-pPv model, particularly for the L2-norm based on the S–C correlation. On the other hand, models with pPv lenses and a pPv-free CMB region (the TH-pPv-extra and TH-pPv-extra100 models) do not reproduce the decrease in the S/P ratio in SP12RTS and the increase in the S–C correlation close to the CMB, resulting in a higher misfit. A spectral decomposition of the different models also suggests that the original TH-pPv model provides the closest fit to the seismic characteristics of SP12RTS at other spherical harmonic degrees (Supplementary Fig. S6). These results imply that the statistical properties of SP12RTS, particularly the positive values of the S–C correlation close to the CMB, are matched best by
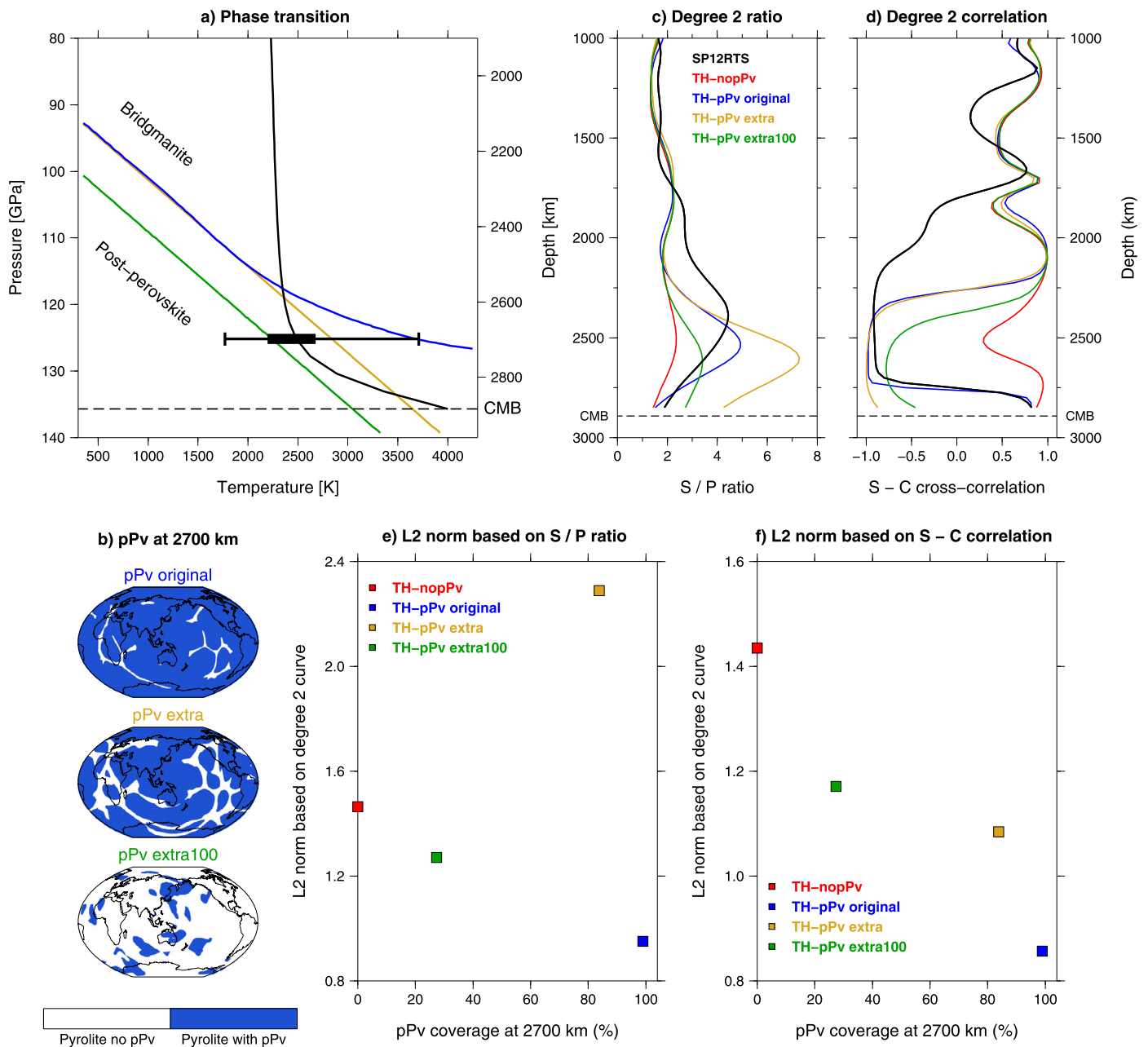
Fig. 10. Effect of (a) different Clapeyron slopes of the phase transition in pyrolite on (b) the amount of pPv in the lower mantle, (c) the S/P ratio and (d) the S–C correlation. (e) and (f) show the L2 norm between SP12RTS and the geodynamic models, based on the degree-2 curves of either (e) the S/P ratio or (f) the S–C correlation. The black line in (a) gives the geotherm of the TH model and the boxcar indicates the 1, 25, 75 and 99% percentiles of the temperature distribution at 2700 km depth. The resulting pPv occurrence maps in (b) contain either pPv everywhere at the CMB for the original mineral physics table (blue) or contain pPv lenses in the colder regions for the extrapolated tables "extra" (yellow) and "extra100" (green). The patterns in the S/P ratio (c) and S–C correlation (d) curves for degree 2 of SP12RTS (black) are matched best by the original mineral physics table (blue).

a pPv-bearing CMB region, an idea that is consistent with work by Cobden et al. (2012) using core diffracted phases.

5. Discussion

We observe only small differences between isochemical and thermochemical models, whereas the areal extent of pPv makes a large difference (Fig. 10). Here, we will first discuss the dominant controls on the S/P ratio and S–C correlation. Then, we discuss the influence of the uncertainties in the mineralogical model on our results. Subsequently, we indicate which seismological features our geodynamic models cannot explain, before ending by considering the implications of our results on the presence of pPv and the nature of lower mantle heterogeneity.

5.1. Dominant controls on the S/P ratio and S–C correlation

The large similarity in S/P ratio and S–C correlation for TH and TC models (despite the presence of large-scale chemical heterogeneity resulting in a different planform of convection) is partly due to the fact that the reparameterisation and tomographic filtering act as low-pass filters (see Section 3). However, the S–C correlation is already markedly negative in high-resolution models with pPv (TH-pPv in Fig. 5a and TC-pPv in Supplementary Fig. S3a). The reason for this is that a similar amount of pPv is present at any given depth in both TH and TC scenarios (Fig. 3). Although the hotter areas have a larger extent in the TC-pPv model, they contain basaltic material, which transforms to pPv at shallower depths

due to the negative Clapeyron slope for basalt at high temperatures (Supplementary Fig. S1b). In addition, the geotherms and temperature distributions of both TH and TC models are similar with the majority of temperatures close to the average (Supplementary Fig. S1). The large similarity in the distribution of pPv results in almost indistinguishable values of the S/P ratio and S–C correlation, with only a small effect from the assumed mantle composition. Tesoniero et al. (2016) came to a similar conclusion, although they considered different compositions for one-dimensional profiles rather than lateral compositional variations.

The assumed CMB temperature has also only a minor effect on the S/P ratio and S–C correlation (Supplementary Fig. S7). Again, the geotherms and temperature distributions throughout the mantle are similar (Supplementary Material and Supplementary Fig. S8). The CMB temperature only affects the excess plume temperatures, not the temperature of subducting material, and slow clusters (hot areas) thus show (slightly) larger differences. However, after filtering, only the slow cluster with $T_{CMB} = 4400$ K is distinguishable (Supplementary Fig. S7c). Consequently, we cannot place constraints on the CMB temperature using our tomographic-geodynamic model comparisons.

Throughout our results, we observe that the areal extent of pPv introduces the largest variations in the S/P ratio and S–C correlation curves (see Fig. 10 and Supplementary Fig. S6). Supplementary Fig. S9 illustrates this further, by plotting the percentage coverage of pPv at any depth versus the S/P ratio and S–C correlation in the high-resolution models. S/P ratios larger than ∼3 and strongly negative values of the S–C correlation are observed only for a pPv coverage of 10–90%. These findings thus imply that in fact it is a partial coverage of pPv (i.e. lateral variations in pPv presence) that produce larger ratios and a negative S–C correlation, rather than pPv being present everywhere or nowhere. This is consistent with the notion that lateral variations in a phase transition have a large effect on averaged quantities (Styles et al., 2011).

Fig. 10f indicates a clear trend between the L2 norm based on the S–C correlation and the percentage coverage of pPv at 2700 km depth. Thermochemical (TC) models and models with different CMB temperatures follow the same trend, indicating again that the lateral areal extent of pPv has the strongest effect on the S/P ratio and S–C correlation. Therefore, these seismic characteristics can only be used to determine the areal extent of pPv and not the composition of the lowermost mantle or CMB temperature.

5.2. Mineral physics uncertainties

We assume a pyrolitic mantle composition, which is a reasonable choice according to recent studies (Davies et al., 2012; Zhang et al., 2013; Shim et al., 2017), and an additional basaltic component in the TC case. Although iron-rich compositions have been suggested as representative for LLVPs, a basaltic composition was favoured by Davies et al. (2012) based on its high density and ability to produce a negative S–C correlation. Given the dominance of pPv on the S/P ratio and S–C correlation, we believe that the main effect of a different mantle composition is to shift the stability field of pPv in depth and thus to change the lateral distribution of pPv. For example, it would occur shallower for MORB or iron-rich material and deeper for harzburgite or Al-rich material (Cobden et al., 2014). The uncertainty in mantle composition is thus addressed by our tests with the extrapolated mineral physics tables, even though these are un-physical.

To convert the temperature and composition fields to seismic velocities, we have opted to use a thermodynamic mineralogical model (Stixrude and Lithgow-Bertelloni, 2011) in which the Clapeyron slope of the brg-pPv transition is non-linear for both pyrolite and basalt. This is in contrast to the general notion of a constant Clapeyron slope assumed in past studies, but the thermodynamic approach is preferable given its self-consistency and the fact that no experimental measurements exist for temperatures above ∼3000 K. In fact, there is no reason to expect a linear Clapeyron slope for the phase transition and our results for the extrapolated tables show that a linear Clapeyron slope does not improve the fit to the seismic data. Furthermore, the values of 3–13 MPa/K in the mineralogical model are consistent with Clapeyron slope estimates from experiments and theoretical calculations (e.g. Hirose, 2006; Stixrude and Lithgow-Bertelloni, 2011; Cobden et al., 2014).

The mineralogical tables are reproducible using an alternative software implementation of the Gibbs free energy minimisation algorithm and equation of state calculations for the same database (Chust et al., 2017). Thus, the database parameters are the primary control on the phase transition depth and the values of the Clapeyron slopes. We may need to re-evaluate the robustness of our findings after additional experimental data at high temperature become available, or for other choices of parameters in the mineralogical tables (e.g. the crystal structure of Ca–Pv (Stixrude et al., 2007)). However, until then, our results show that for widely-used parameters, a pPv-bearing CMB region explains several lower mantle characteristics of global tomography models. This is consistent with work by Mosca et al. (2012) and Cobden et al. (2012), who, based on a large range of mineralogical models, also favoured models with pPv to explain lower mantle seismological observations.

5.3. Mid-mantle discrepancy

A discrepancy remains between SP12RTS and the geodynamic models between 1800 km and 2300 km depth, where SP12RTS features an increased S/P ratio and the onset of a negative S–C correlation (Fig. 7b). Given that we account for the limited tomographic resolution, we cannot explain this discrepancy with pPv, or more accurately, not with the parameters constraining the stability field of pPv in the different mineral physics tables. As mentioned before, the stability field of pPv is not well constrained in high-pressure, high-temperature experiments, even for pure MgSiO$_3$ (Cobden et al., 2014). Differences of 5–10 GPa in the transition pressure exist due to the pressure standard used in experiments (Tsuchiya et al., 2004; Hirose, 2006) and additional errors of 5–10 GPa could be introduced due to reversing the phase boundary. Therefore, it is possible that pPv is present at (slightly) shallower depths than currently assumed. However, given the small changes in peak depth for different Clapeyron slopes (Fig. 10), we question whether it would explain the discrepancy entirely.

The iron spin transition provides another explanation for the discrepancy at 1800–2300 km depth, as this gradually affects seismic properties without producing sharp discontinuities (e.g. Stackhouse et al., 2007; Wentzcovitch et al., 2009). The effect of the spin transition in bridgmanite remains debated, but for ferropericlase, the spin transition has a clear effect on the seismic velocities. It primarily changes the bulk modulus (e.g. Wentzcovitch et al., 2009; Marquardt et al., 2009), which results in a drop of V_P with no change in V_S; hence the S/P ratio increases and the S–C correlation becomes negative. The depth range where this effect is expected depends on temperature, occurring typically deeper and over a wider depth range with increasing temperature, e.g. around 75 GPa (1700 km depth) for a temperature of 2500 K (Marquardt et al., 2009). This effect of the spin transition, unaccounted for in the mineralogical model employed here, could help to resolve the discrepancy at mid-mantle depths. Whether incorporating changes in the oxidation state of iron, as suggested recently by Shim et al. (2017), or shear softening of Ca–Pv (Stixrude et al., 2007) improves the fit between SP12RTS and the geodynamic models further, remains to be seen. Finally, we cannot exclude the possibility that a negative S–C correlation at these depths (1800–2300 km) is due to

the presence of chemical heterogeneity, i.e. tall, chemically distinct LLVPs. Although it would be difficult to predict their exact composition, the presence of MORB or iron-rich material (due to the accumulation of subducted crust or core-reaction products) would cause the pPv transition to occur at shallower depth, thereby reducing the mid-mantle discrepancy.

5.4. Implications for lower mantle structures

We show that the features of SP12RTS are best reproduced by the original mineral physics table, and thus by a pPv-bearing CMB region (Fig. 10c–f). We propose two different scenarios to achieve this, based on our tomographic-geodynamic comparisons. One possibility is that the Clapeyron slope of the brg-pPv transition in pyrolite shallows at high temperature, as predicted by the original mineral physics table (Supplementary Fig. S1a). Alternatively, the Clapeyron slope has a higher, constant slope, but the entire stability field of pPv is shifted to shallower depths than has been considered here. A shallower stability field of pPv would likely give rise to a shallower peak depth of the S/P ratio. This may thus improve the mismatch in peak depth currently observed between SP12RTS and the geodynamic models with pPv (Fig. 7), given that no improvement is observed for a change in the CMB temperature. To distinguish between the two proposed scenarios, mineral physics measurements of bridgmanite/pPv at high temperature (>3000 K) and pressures above 115 GPa are required.

For a pPv-bearing CMB region, pPv needs to be stable at temperatures as high as 3600–4000 K. Whether such temperatures are too high remains debated, as solidus temperatures vary between $\sim$4150 K (Andrault et al., 2011) and 3570 $\pm$ 200 K (Nomura et al., 2014). Nevertheless, our results for different CMB temperatures indicate that even for a CMB temperature of 3600 K, the characteristics of SP12RTS are reproduced best by models with pPv everywhere, including inside the LLVPs (Supplementary Fig. S7). The occurrence of pPv within the LLVPs remains debated (Garnero et al., 2016), complicated by uncertainties in estimates of its stability field and its dependence on chemical composition (Cobden et al., 2014). However, recent normal-mode studies (Koelemeijer et al., 2017) and body-wave studies (Cobden et al., 2012) have favoured the presence of pPv within the LLVPs. When considering the presence of pPv inside tomographically-imaged LLVPs, it is also important to keep in mind that they may contain smaller-scale features (i.e. cold regions containing pPv), which are lost due to the limited resolution in tomography.

For the two possible scenarios described above, it is unlikely that the geotherm crosses the phase boundary a second time just above the CMB for CMB temperatures of 3600–4400 K. Hence, seismic observations of paired discontinuities can no longer be explained by a double crossing of the phase transition, as assumed by previous authors in efforts to constrain the CMB heat flux (e.g. Hernlund et al., 2005; Lay et al., 2008). Instead, the stishovite-seifertite transition in the silicate system could potentially explain these observations (Grocholski et al., 2013). In addition, the temperature–pressure dependence of the Clapeyron slope may reconcile differences observed in the depth of the D'' discontinuity without the need to invoke local chemical heterogeneity.

6. Conclusions

By comparing the statistical properties of tomographic model SP12RTS with synthetic tomography models derived from geodynamic simulations with and without post-perovskite and/or chemical heterogeneity, we have shown that:

1. We can identify the signature of pPv in global tomography models, even when accounting for the limited resolution of seismic tomography.
2. Lateral variations in the presence of pPv give rise to a negative S–C correlation and high S/P ratio below 2300 km depth, explaining seismic characteristics.
3. Due to the dominant control of pPv, one cannot constrain the composition of the lowermost mantle using seismic observations of the S/P ratio and S–C correlation.
4. The characteristics of SP12RTS are reproduced best for a CMB region covered by pPv, implying the presence of pPv inside the LLVPs.
5. Two scenarios are proposed for the brg-pPv transition: a shallowing of the Clapeyron slope at high temperature or a shallower stability field for pPv.
6. Our comparisons cannot be used to constrain the CMB temperature due to our limited tomographic resolution.
7. Observed differences in the predicted depth of the negative S–C correlation, across a number of studies, are likely related to the data types used in the inversion procedures, with body-wave models artificially smearing the signal upwards to shallower depths.
8. A discrepancy between SP12RTS and geodynamic predictions remains at mid-mantle depths (1800–2300 km), which could be due to uncertainties in the mineralogical model, unaccounted effects of the spin transition and/or the presence of shallower chemical heterogeneity.

Throughout our comparisons, we have stressed the importance of tomographic filtering. This aids not only the identification of robust features in tomographic models, but it is also essential for meaningful comparisons between tomographic and geodynamic models. The tomographic filter of SP12RTS, which filters both V_S and V_P structures jointly without any a-priori constraints, has an improved resolution close to the CMB compared to other studies and has been developed specifically to enable comparisons of seismic velocity ratios and correlations. Consequently, interested parties are encouraged to incorporate the SP12RTS filtering software (available online).

Despite the uncertainties in mantle composition and assumptions in the geodynamic modelling, we have demonstrated that a pPv-bearing CMB region is preferred for explaining the decrease in the S/P ratio towards the CMB. The inference that pPv is present everywhere close to the CMB, also inside the LLVPs, should not be ignored as a possibility in future studies. In addition, our study indicates the potential for constraining the Clapeyron slope of the brg-pPv phase transition using global tomography, especially if future studies incorporate a denser depth parameterisation in the lowermost mantle.

Acknowledgements

Appendix A. Supplementary material

Supplementary material related to this article can be found online at https://doi.org/10.1016/j.epsl.2018.04.056.

References

Andrault, D., Bolfan-Casanova, N., Nigro, G.L., Bouhifd, M.A., Garbarino, G., Mezouar, M., 2011. Solidus and liquidus profiles of chondritic mantle: implication for melting of the Earth across its history. Earth Planet. Sci. Lett. 304 (1–2), 251–259.

Baumgardner, J.R., 1985. Three-dimensional treatment of convective flow in the Earth's mantle. J. Stat. Phys. 39 (5), 501–511.

Chust, T.C., Steinle-Neumann, G., Dolejs, D., Schuberth, B.S., Bunge, H.P., 2017. MMA-EoS: a computational framework for mineralogical thermodynamics. J. Geophys. Res. 122, 9881–9920.

Cobden, L., Mosca, I., Trampert, J., Ritsema, J., 2012. On the likelihood of post-perovskite near the core–mantle boundary: a statistical interpretation of seismic observations. Phys. Earth Planet. Inter. 210, 21–35.

Cobden, L., Thomas, C., Trampert, J., 2014. Seismic detection of post-perovskite inside the Earth. In: The Earth's Heterogeneous Mantle.

Davies, D.R., Davies, J.H., Bollada, P.C., Hassan, O., Morgan, K., Nithiarasu, P., 2013. A hierarchical mesh refinement technique for global 3D spherical mantle convection modelling. Geosci. Model Dev. 6, 1095–1107.

Davies, D.R., Goes, S., Davies, J.H., Schuberth, B.S.A., Bunge, H., Ritsema, J., 2012. Reconciling dynamic and seismic models of Earth's lower mantle: the dominant role of thermal heterogeneity. Earth Planet. Sci. Lett. 353, 253–269.

Davies, D.R., Goes, S., Lau, H.C.P., 2015. Thermally dominated deep mantle LLSVPs: a review. In: Khan, A., Deschamps, F. (Eds.), The Earth's Heterogeneous Mantle. Springer International Publishing, pp. 441–477.

Della Mora, S., Boschi, L., Tackley, P., Nakagawa, T., Giardini, D., 2011. Low seismic resolution cannot explain S/P decorrelation in the lower mantle. Geophys. Res. Lett. 38 (12).

Garnero, E., McNamara, A., Shim, S.-H., 2016. Continent-sized anomalous zones with low seismic velocity at the base of Earth's mantle. Nat. Geosci. 9 (7), 481–489.

Grocholski, B., Shim, S.-H., Prakapenka, V., 2013. Stability, metastability, and elastic properties of a dense silica polymorph, seifertite. J. Geophys. Res. 118 (9), 4745–4757.

Hernlund, J., Thomas, C., Tackley, P., 2005. A doubling of the post-perovskite phase boundary and structure of the Earth's lowermost mantle. Nature 434 (7035), 882–886.

Hirose, K., 2006. Postperovskite phase transition and its geophysical implications. Rev. Geophys. 44.

Ishii, M., Tromp, J., 1999. Normal-mode and free-air gravity constraints on lateral variations in velocity and density of Earth's mantle. Science 285 (5431), 1231.

Karato, S.-i., Karki, B.B., 2001. Origin of lateral variation of seismic wave velocities and density in the deep mantle. J. Geophys. Res. 106 (R10), 21771–21783.

Koelemeijer, P., Deuss, A., Ritsema, J., 2013. Observations of core–mantle boundary Stoneley modes. Geophys. Res. Lett. 40 (11), 2557–2561.

Koelemeijer, P., Deuss, A., Ritsema, J., 2017. Density structure of Earth's lowermost mantle from Stoneley mode splitting observations. Nat. Commun. 8, 15241.

Koelemeijer, P., Ritsema, J., Deuss, A., Van Heijst, H.-J., 2016. SP12RTS: a degree-12 model of shear-and compressional-wave velocity for Earth's mantle. Geophys. J. Int. 204 (3), 1024–1039.

Lau, H.C., Mitrovica, J.X., Davis, J.L., Tromp, J., Yang, H.-Y., Al-Attar, D., 2017. Tidal tomography constrains Earth's deep-mantle buoyancy. Nature 551 (7680), 321.

Lay, T., Hernlund, J., Buffett, B., 2008. Core–mantle boundary heat flow. Nat. Geosci. 1 (1), 25–32.

Lekić, V., Cottaar, S., Dziewonski, A., Romanowicz, B., 2012. Cluster analysis of global lower mantle tomography: a new class of structure and implications for chemical heterogeneity. Earth Planet. Sci. Lett. 357, 68–77.

Malcolm, A.E., Trampert, J., 2011. Tomographic errors from wave front healing: more than just a fast bias. Geophys. J. Int. 185 (1), 385–402.

Marquardt, H., Speziale, S., Reichmann, H.J., Frost, D.J., Schilling, F.R., 2009. Single-crystal elasticity of (Mg 0.9 Fe 0.1) O to 81 GPa. Earth Planet. Sci. Lett. 287 (3), 345–352.

Masters, G., Laske, G., Bolton, H., Dziewonski, A., 2000. The relative behavior of shear velocity, bulk sound speed, and compressional velocity in the mantle: implications for chemical and thermal structure. Geophys. Monogr. AGU 117, 63–87.

Mosca, I., Cobden, L., Deuss, A., Ritsema, J., Trampert, J., 2012. Seismic and mineralogical structures of the lower mantle from probabilistic tomography. J. Geophys. Res. 117 (B6), B06304.

Moulik, P., Ekström, G., 2016. The relationships between large-scale variations in shear velocity, density, and compressional velocity in the Earth's mantle. J. Geophys. Res. 121 (4), 2737–2771.

Murakami, M., Hirose, K., Kawamura, K., Sata, N., Ohishi, Y., 2004. Post-perovskite phase transition in MgSiO$_3$. Science 304 (5672), 855.

Nomura, R., Hirose, K., Uesugi, K., Ohishi, Y., Tsuchiyama, A., Miyake, A., Ueno, Y., 2014. Low core–mantle boundary temperature inferred from the solidus of pyrolite. Science 1248186.

Oganov, A., Ono, S., 2004. Theoretical and experimental evidence for a post-perovskite phase of MgSiO$_3$ in Earth's D″ layer. Nature 430 (6998), 445–448.

Ritsema, J., Deuss, A., van Heijst, H.-J., Woodhouse, J.H., 2011. S40RTS: a degree-40 shear-velocity model for the mantle from new Rayleigh wave dispersion, teleseismic traveltime and normal-mode splitting function measurements. Geophys. J. Int. 184 (3), 1223–1236.

Ritsema, J., McNamara, A.K., Bull, A.L., 2007. Tomographic filtering of geodynamic models: implications for model interpretation and large-scale mantle structure. J. Geophys. Res. 112 (B1).

Romanowicz, B., 2001. Can we resolve 3D density heterogeneity in the lower mantle? Geophys. Res. Lett. 28 (6), 1107–1110.

Schuberth, B., Bunge, H.-P., Ritsema, J., 2009a. Tomographic filtering of high-resolution mantle circulation models: can seismic heterogeneity be explained by temperature alone? Geochem. Geophys. Geosyst. 10 (5), Q05W03.

Schuberth, B., Bunge, H.-P., Steinle-Neumann, G., Moder, C., Oeser, J., 2009b. Thermal versus elastic heterogeneity in high-resolution mantle circulation models with pyrolite composition: high plume excess temperatures in the lowermost mantle. Geochem. Geophys. Geosyst. 10 (1), Q01W01.

Seton, M., Müller, R., Zahirovic, S., Gaina, C., Torsvik, T., Shephard, G., Talsma, A., Gurnis, M., Turner, M., Maus, S., et al., 2012. Global continental and ocean basin reconstructions since 200 Ma. Earth-Sci. Rev. 113 (3), 212–270.

Shim, S.-H., Grocholski, B., Ye, Y., Alp, E.E., Xu, S., Morgan, D., Meng, Y., Prakapenka, V.B., 2017. Stability of ferrous-iron-rich bridgmanite under reducing midmantle conditions. Proc. Natl. Acad. Sci. USA 201614036.

Simmons, N.A., Forte, A.M., Boschi, L., Grand, S.P., 2010. GyPSuM: a joint tomographic model of mantle density and seismic wave speeds. J. Geophys. Res. 115 (B12).

Stackhouse, S., Brodholt, J.P., Price, G.D., 2007. Electronic spin transitions in iron-bearing MgSiO$_3$ perovskite. Earth Planet. Sci. Lett. 253 (1), 282–290.

Stixrude, L., Lithgow-Bertelloni, C., 2011. Thermodynamics of mantle minerals: II. Phase equilibria. Geophys. J. Int. 184 (3), 1180–1213.

Stixrude, L., Lithgow-Bertelloni, C., Kiefer, B., Fumagalli, P., 2007. Phase stability and shear softening in CaSiO$_3$ perovskite at high pressure. Phys. Rev. 75 (2), 024108.

Styles, E., Davies, D.R., Goes, S., 2011. Mapping spherical seismic into physical structure: biases from 3D phase-transition and thermal boundary-layer heterogeneity. Geophys. J. Int. 184 (3), 1371–1378.

Su, W., Dziewonski, A., 1997. Simultaneous inversion for 3-D variations in shear and bulk velocity in the mantle. Phys. Earth Planet. Inter. 100 (1–4), 135–156.

Tesoniero, A., Cammarano, F., Boschi, L., 2016. S-to-P heterogeneity ratio in the lower mantle and thermo-chemical implications. Geochem. Geophys. Geosyst. 17 (7), 2522–2538.

Trampert, J., Deschamps, F., Resovsky, J., Yuen, D., 2004. Probabilistic tomography maps chemical heterogeneities throughout the lower mantle. Science 306 (5697), 853.

Tsuchiya, T., Tsuchiya, J., Umemoto, K., Wentzcovitch, R., 2004. Phase transition in MgSiO$_3$ perovskite in the Earth's lower mantle. Earth Planet. Sci. Lett. 224 (3–4), 241–248.

Wentzcovitch, R., Justo, J., Wu, Z., da Silva, C.R., Yuen, D., Kohlstedt, D., 2009. Anomalous compressibility of ferropericlase throughout the iron spin cross-over. Proc. Natl. Acad. Sci. USA 106 (21), 8447–8452.

Wessel, P., Smith, W.H.F., Scharroo, R., Luis, J., Wobbe, F., 2013. Generic mapping tools: improved version released. Eos Trans. AGU 94 (45), 409–410.

Wookey, J., Stackhouse, S., Kendall, J.-M., Brodholt, J., Price, G.D., 2005. Efficacy of the post-perovskite phase as an explanation for lowermost-mantle seismic properties. Nature 438 (7070), 1004–1007.

Zaroli, C., Koelemeijer, P., Lambotte, S., 2017. Toward seeing the Earth's interior through unbiased tomographic glasses. Geophys. Res. Lett. 44 (22).

Zhang, Z., Stixrude, L., Brodholt, J., 2013. Elastic properties of MgSiO$_3$-perovskite under lower mantle conditions and the composition of the deep Earth. Earth Planet. Sci. Lett. 379, 1–12.